Mechanical Systems and Signal Processing 156 (2021) 107607

Contents lists available at ScienceDirect

Mechanical Systems and Signal Processing

journal homepage: www.elsevier.com/locate/ymssp

Simultaneous vibration reduction and energy harvesting of a nonlinear oscillator using a nonlinear electromagnetic vibration absorber-inerter

Paul Kakou, Oumar Barry *

Department of Mechanical Engineering, Virginia Tech, Blacksburg, VA 24060, United States

ARTICLE INFO

Article history:
Received 16 October 2020
Received in revised form 15 December 2020
Accepted 1 January 2021

Keywords:
Nonlinear oscillator
Nonlinear vibration control
Energy harvesting
Inerter
Electro-magnetic transducer
RLC circuit
Harmonic balance method with arc-length continuation

ABSTRACT

Recently, considerable attention has been given to electromagnetic resonant shunt tuned mass damper-inerters (ERS-TMDI) for simultaneous vibration mitigation and energy harvesting. The application of this design is already well-established for linear structures, however, it is not extensively explored for nonlinear structures. This work, for the first time, aims to achieve both vibration mitigation and energy harvesting for nonlinear oscillating structures using a single device. For this, a novel nonlinear electromagnetic resonant shunt tuned mass damper-inerter (NERS-TMDI) is proposed with two different configurations. The proposed NERS-TMDI is coupled to a nonlinear oscillator via linear and nonlinear springs. For the first configuration, the electromagnetic and the inerter devices are grounded on one side and connected to the nonlinear vibration absorber on the other side. In the second configuration, the electromagnetic device is placed between the nonlinear vibration absorber and the primary structure. The nonlinear governing equations of motion are solved analytically using the method of harmonic balance in conjunction with the fixed arc-length continuation method. The analytical approach is validated using numerical simulations. A detailed parametric analysis for both configurations is conducted to identify the key design parameters that render the best performance of the NERS-TMDI. The results show that the proposed NERS-TMDI configurations perform better than the existing approaches, including the nonlinear tuned mass damper (NTMD), and the ERS-TMDI, in terms of vibration control. The results also show that the first configuration of NERS-TMDI always performs better for simultaneous vibration mitigation and energy harvesting than the second configuration of NERS-TMDI. This implies that grounding the electromagnetic transducer extends the range of effectiveness of the NERS-TMDI. Further, a sensitivity analysis on the optimal Configuration-1 showed that the NERS-TMDI is robust to variations in nonlinear stiffness, but its performance degrades for variations in inertance, resistance, inductance, and capacitance. Additionally, a parametric study demonstrates that higher values of nonlinear stiffness, inertance, and resistance, and lower values of inductance and capacitance render an optimal design of the Configuration-1 of the NERS-TMDI for energy harvesting. The findings are very promising and open a horizon of future opportunities to optimize the design of the NERS-TMDI for superior performance.

---

* Corresponding author.
E-mail address: obarry@vt.edu (O. Barry).

https://doi.org/10.1016/j.ymssp.2021.107607
0888-3270/© 2021 Published by Elsevier Ltd.

1. Introduction

Development of a better model for engineering structures and components is a crucial step towards vibration control and energy harvesting. These models can exhibit only linear or linear and nonlinear characteristics of the system. However, it has been observed that linear models fail to capture the essential dynamics of the system with large amplitude oscillations and therefore, nonlinear models need to be considered for the analysis. As an example, in aerospace engineering, three-axis gimbal systems are installed on UAVs to track moving targets in military applications. In the earlier studies, the design and vibration control of the gimbal systems have been performed using linear models [1,2]. However, Altan and Hacioglu [3,4] showed that using a nonlinear model in the dynamical analysis significantly helps to improve the design of a control strategy for robustness and stability. Another example relates to the modelling and design of a vibration absorber for power lines. When left uncontrolled, wind induced vibrations in power lines cause structural damages, further affecting businesses, factories, and local communities. Earlier studies suggest that nonlinear models of cable vibration and cable-wind interaction are an essential step to develop an effective nonlinear passive vibration absorber [5,6]. The aforementioned systems also have some energy requirements. Gimbal systems need power to take advantage of their built-in controller and power lines rely on sensors and wireless devices for structural health monitoring. To this end, the ability to harvest energy from the vibrating structures is of practical importance. Though, there are systems that achieve both, i.e., vibration control and energy harvesting for linear models [7–9], an optimized design for vibration control and energy harvesting for a nonlinear structure has not been extensively reported yet. This is the focus of the current work.

There are several approaches which have been employed in the literature to control/suppress vibrations in engineering structures and components without and with energy harvesting. However, for the sake of completeness, we present relevant literature on these methods and their shortcomings. Frahm *et al.* [10] originally designed tuned-mass-dampers (TMD) to mitigate mechanical vibrations. Since this initial development, several researchers have optimized linear vibration control solutions based on tuned dampers via passive [11–14], semi-active [15–17] and active [18–20] means. TMD are used for their simplicity, ease of installation and effectiveness. However, TMD tend to be effective on a narrow range of operating frequency [21,22]. One strategy to extend the performance of TMD is to increase their overall weight. However, increasing the actual mass of TMD is not feasible as well as not-cost effective for many engineering applications. To resolve this issue, investigators have developed an inerter device, which is a two terminal flywheel mechanical device that generates a force proportional to the relative acceleration of its two terminals [23,24]. TMD have successfully incorporated inerters in their design [25–30] for improved performance. Nonetheless, TMD are designed solely for vibration control.

Alternative solutions such as shunt dampers (SD) have also been considered in the literature for vibration control. In 1979, Forward *et al.* [31] were the first ones to demonstrate the use of passive circuit shunting for narrow-band reduction of resonant mechanical response. Further, Hagood and von Flotow [32] theoretically and experimentally proved that piezoelectric shunt with an RL circuit will act as a TMD. The use of SD using piezoelectric material and electromagnetic transducer is well-established in the literature [33–36]. For both piezoelectric and electromagnetic designs, the resistive shunt exhibits viscous damping effects, while the inductor and the resistor introduce an electrical resonance, and acts like a mechanical vibration absorber. SD also provide vibration suppression for several energy levels and for a comparatively wider frequency range as compared to TMD [37]. Note that these physical behaviors of SD can considerably enhance the performance of vibration control devices [38]. Further, it has been noted that using SD, it is possible to achieve both vibration control and energy harvesting. For instance, using the electromagnetic device in SD, some of the energy that was originally dissipated by the damping element of TMD, can be recovered electrically. With this objective, investigators have developed electromagnetic resonant shunt tuned mass dampers (ERS-TMD) [39] and more recently, electromagnetic resonant shunt tuned mass damper with inerters (ERS-TMDI) [40,41] to take advantage of the effective mass properties of the inerter devices. Following these efforts, Joubaneh and Barry [42] recently optimized the conventional design of ERS-TMDI by grounding the electromagnetic transducer, and successfully showed that significant vibration control and energy harvesting could be achieved simultaneously for linear oscillators. They showed that the optimized design of ERS-TMDI performs better than other existing configurations of ERS-TMDI.

Note that in the aforementioned studies, linear vibration control strategies have been developed for structures with linear characteristics. However, engineering structures exhibit nonlinear behavior due to geometric, material, and nonlinear external force characteristics [43,44], and linear control methods will not be able to perform efficiently on these systems. Therefore, to recover the control performance of TMD and ERS-TMDI, mechanisms, which can deliver nonlinear reacting forces, can be added to the system. With this motivation, Sun *et al.* [45] and Habib *et al.* [46] designed nonlinear vibration absorbers to enhance the performance of TMD by extending the concept of Den's Hartog equal peak method for nonlinear oscillations. They observed that nonlinear tuned mass dampers (NTMD) perform better than linear TMD to mitigate vibrations in primary nonlinear systems. However, to the authors' best knowledge, the corresponding nonlinear device for ERS-TMDI has not been reported yet.

This work, for the first time, aims to fulfill this gap by designing an optimum nonlinear electromagnetic resonant shunt tuned mass damper-inerter (NERS-TMDI) for vibration control and energy harvesting. For this purpose, we modify the optimal ERS-TMDI by including a nonlinear spring in ERS-TMDI, making it a nonlinear ERS-TMDI (NERS-TMDI). We study the proposed NERS-TMDI in two different configurations (i) a grounded electromagnetic resonant shunt tuned mass damper-inerter in which the electromagnetic transducer is grounded on one side and connected to the vibration absorber's mass on the other [42], and (ii) a sandwiched electromagnetic shunt resonant tuned damper-inerter [41]. The NERS-TMDI is connected to a Duffing oscillator, and the overall system is subjected to a harmonic excitation. Following Habib *et al.* [46], the NERS-TMDI is comprised of a cubic nonlinear stiffness to match the nonlinear stiffness of the primary structure. The nonlinear governing equations of motion are solved analytically using the method of harmonic balance in concurrence with the fixed arc-continuation method [47]. The results are validated using numerical simulations. The proposed NERS-TMDI configurations performance are compared to the conventional NTMD, as well as the optimal linear ERS-TMDI. A detailed parametric analysis is conducted to evaluate the forcing amplitude range for each configuration in terms of vibration control and energy harvesting. The analysis also helps to determine the impact of the nonlinear stiffness, the inertance, and the RLC circuit elements on the performance of the NERS-TMDI.

The remainder of the paper is organized as follows. In Section 2, the mathematical models for the two configurations of the NERS-TMDI are presented briefly along with the analytical solution approach. A detailed numerical analysis of the NERS-TMDI configurations is presented along with the comparisons with NTMD and ERS-TMDI in Section 3. This includes the energy harvesting potential of the NERS-TMDI, the influence of the nonlinear stiffness, the inertance, and the RLC circuit parameters. In Section 4, a brief discussion of the main results is presented. Finally, some conclusions are drawn in Section 5.

2. Mathematical modeling

The schematics of the modified optimal configurations of ERS-TMDI [41,42] are shown in Fig. 1. In the models, m_s represents the mass of the primary structure, k_s and k_{sn} represent the linear and nonlinear springs of the primary structure, respectively, and c_s represents the viscous damping coefficient of the primary structure. A nonlinear spring is added to the traditional optimal configurations for ERS-TMDI [41,42] making them nonlinear ERS-TMDI (NERS-TMDI). The primary structure is connected to the tuned mass of NERS-TMDI, m_t, via a linear and a nonlinear spring element, k_t and k_{tn}, respectively, along with a linear viscous damping element of coefficient c_t.

Traditionally, TMD are used to dissipate energy from the primary system and, hence, to control vibration. However, in the NERS-TMDI, we replace the viscous damping of the TMD with an electromagnetic resonant shunt component which further implies $c_t = 0$ for the proposed design. In the current work, the primary structure is considered to be in the form of a Duffing oscillator, and thus exhibits cubic nonlinearity for k_{sn}. Since a better performance of the absorber requires that it has a similar nonlinear characteristic as the primary structure [45,46], we assume cubic nonlinearity for k_{tn} too. To relax the tradeoff between energy harvesting and vibration control, the electromagnetic transducer, e_{EMF}, is grounded on one side and connected to m_t on the other side for Configuration-1 (Fig. 1-(a)), while for Configuration-2 it is placed between m_t and m_s (Fig. 1-(b)). The resistance, the inductance, and the capacitance of the electrical circuit are denoted by R, L, and C, respectively, whereas k_v and k_f represent the voltage constant and the force constant of the transducer, respectively. For the current analysis, we assume an ideal transducer without any energy loss, which leads to the identity $k_v = k_f$. Using Newton's method, the governing equations of motion can be derived and are given for Configuration-1:

$$m_s\ddot{x}_s + c_s\dot{x}_s + k_s x_s + k_{sn}x_s^3 - k_t(x_t - x_s) - k_{tn}(x_t - x_s)^3 = F_w, \tag{1a}$$

$$(m_t + b)\ddot{x}_t + k_t(x_t - x_s) + k_{tn}(x_t - x_s)^3 + k_f I = 0, \tag{1b}$$

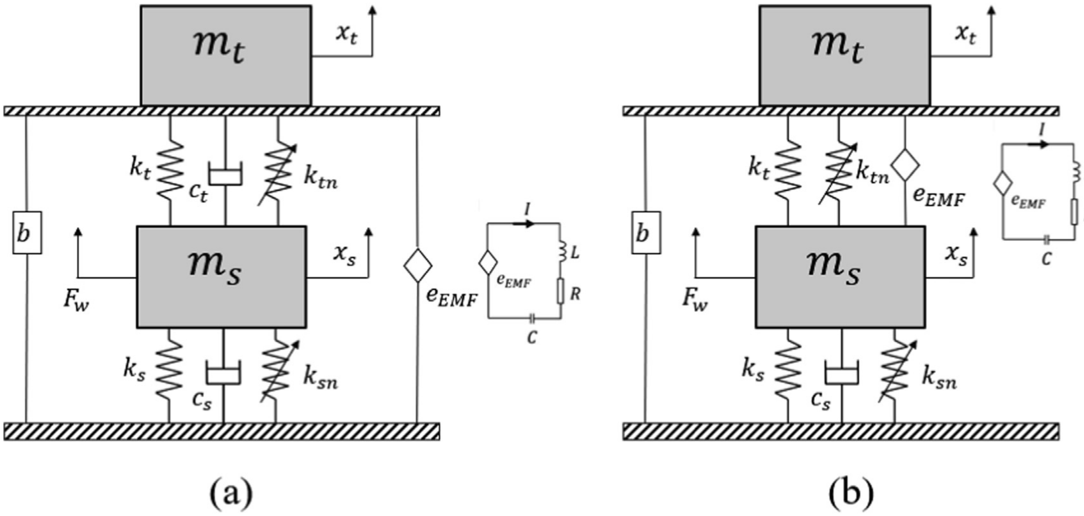

Fig. 1. Schematic of the primary mass attached to NERS-TMDI for (a) Configuration-1 and for (b) Configuration-2.

$$-k_v\dot{x}_t + RI + L\dot{I} + \frac{1}{C}\int Idt = 0, \tag{1c}$$

and for Configuration-2:

$$m_s\ddot{x}_s + c_s\dot{x}_s + k_sx_s + k_{sn}x_s^3 - k_t(x_t - x_s) - k_{tn}(x_t - x_s)^3 + k_fI = F_w, \tag{2a}$$

$$(m_t + b)\ddot{x}_t + k_t(x_t - x_s) + k_{tn}(x_t - x_s)^3 - k_fI = 0, \tag{2b}$$

$$k_v(\dot{x}_t - \dot{x}_s) + RI + L\dot{I} + \frac{1}{C}\int Idt = 0, \tag{2c}$$

where F_w represents an external excitation, which can be in the form of harmonic, base or random excitation, and x_t, x_s and I represent the motions of the primary mass, the absorber mass and the variation in the current. However, in this study, unless otherwise stated, we consider harmonic excitation in the form of $F_w = F\sin(\omega t)$ applied to the system with F as the amplitude of the harmonic excitation and ω is the excitation frequency. To get the solution for the coupled nonlinear differential equations of motion for Configuration-1 and Configuration-2, we use the harmonic balance method (HBM). For this purpose, we assume the solution of the primary mass, the absorber mass and the variation in current in the form as:

$$x_s = A_{s0} + A_s\cos(\omega t) + B_s\sin(\omega t) + A_{s3}\cos(3\omega t) + B_{s3}\sin(3\omega t), \tag{3a}$$

$$x_t = A_{t0} + A_t\cos(\omega t) + B_t\sin(\omega t) + A_{t3}\cos(3\omega t) + B_{t3}\sin(3\omega t), \tag{3b}$$

$$I = A_{i0} + A_i\cos(\omega t) + B_i\sin(\omega t) + A_{i3}\cos(3\omega t) + B_{i3}\sin(3\omega t). \tag{3c}$$

It should be noted that the assumed solutions include constant terms for DC and asymmetric motions along with simple and higher harmonics of cosine and sine terms due to the cubic nonlinearity in the system. These assumed solutions are substituted in Eqs. (1) and (2). On collecting coefficients of cosine and sine terms for each harmonic along with constant terms, we get fifteen nonlinear algebraic equations for both configurations. These equations are very long, and hence, not reported here for the sake of brevity. Further, these equations can be solved numerically for a given value of forcing amplitude F and excitation frequency ω, and the solutions for both configurations can be obtained utilising Eq. (3). In particular, we use the fixed arc-length continuation scheme developed in [47] to solve these nonlinear algebraic simultaneous equations.

The solution to these nonlinear equations helps us to determine the displacement of the primary source as well as the amount of current generated in the electromagnetic device. In addition to the governing equations of motion, we also introduce the following expression to define the energy harvested by the NERS-TMDI as follows [6]:

$$E_{har,\%} = 100\frac{\int_0^t (RI^2(\tau))d\tau}{\int_0^t F_w\dot{x}_s(\tau)d\tau} \tag{4}$$

In the above equation, $E_{har,\%}$ represents the energy harvested by the system.

3. Results

In this section, we start with validating our analytical results obtained using the HBM to establish their accuracy. Then, the proposed configurations for the NERS-TMDI are compared to the conventional NTMD and ERS-TMDI in terms of relative operational forcing range and vibration amplitude control. Further, Configuration-1 and Configuration-2 are also compared to each other with varying values of forcing amplitude to establish an effective optimized configuration. Finally, a parametric analysis is presented to determine the key parameters of the NERS-TMDI [46].

3.1. Validation of analytical results from HBM

As discussed earlier, the first part of our analysis is to validate the analytical results obtained using HBM, i.e., Eq. (3) by comparing them against the numerical results of Eqs. (1) and (2). The comparison between the analytical and numerical simulations are presented for the parameter values listed in Table 1. The NERS-TMDI is attached to Duffing oscillator with parameters $m_s = 1\ kg$, $k_s = 1\ N/m$, $k_{sn} = 1\ N/m^3$ and $c_s = 0.01\ Ns/m$. For the numerical simulations, we have used the built-in command 'ode45' in MATLAB with high values of absolute tolerance and relative tolerance ($1e^{-8}$).

Table 1
Parameters for Configuration-1 of the NERS-TMDI.

$m_t[kg]$	$b[kg]$	$k_t[N/m]$	$k_{tn}[N/m^3]$	k_f	$R(\Omega)$	$L(H)$	$C[F]$
0.02	0.02	0.0423	0.00074	0.0596	0.3657	0.9649	1.02

To compare the analytical solutions and numerical simulations, we have used the frequency response of the NERS-TMDI. Also, for the sake of brevity, we only present this comparison for Configuration-1 which is shown in Fig. 2. From Fig. 2, we can observe that there is an excellent agreement between both approaches with a maximum error of 0.4% and thus, validating our analytical solution. Therefore, in the remainder of the analysis, we will use the analytical solutions unless otherwise stated.

3.2. Performance analysis of NERS-TMDI configurations

Having established the accuracy of analytical solutions, the next step is to determine the effectiveness of the proposed NERS-TMDI configurations over existing methods, i.e., NTMD and ERS-TMDI. For this, we compare the frequency response curve of the primary system for both configurations of the proposed NERS-TMDI with the NTMD and the ERS-TMDI. These comparisons with TMD and ERS-TMDI are

shown in Figs. 3 and 4, respectively. The linear parameters for Configuration-1 and Configuration-2 were tuned using the optimal methods discussed in Joubaneh *et al.* [42] and Luo *et al.* [41], respectively. The nonlinear components of each configuration of NERS-TMDI, as well as the nonlinear parameters of the NTMD, were tuned using the methodology described in Habib *et al.* [46]. The tuning parameters are determined based on the parameters of the Duffing oscillator as described in Section 3.1. The mechanical and electrical parameters of Configuration-1, Configuration-2, and the NTMD are described in Tables 1–3, respectively, and will be used for the remainder of this analysis. Fig. 3 (a) and (b) show the response of the primary system for each configuration and the conventional NTMD with forcing amplitudes of $F = 0.05\ N$ and $F = 0.062\ N$, respectively. From these figures, we can observe that Configuration-1 displays superior performance in terms of vibration mitigation of the primary structure nearly for all values of frequency in the frequency spectrum, as compared to the conventional NTMD and Configuration-2. Furthermore, the effective frequency bandwidth of both configurations of the NERS-TMDI is widened in comparison to the NTMD. We emphasize that this observation further implies that the electromagnetic resonant shunt damping component in NERS-TMDI provides better vibration control than the classical NTMD with viscous damping. In Fig. 3(a), for $F = 0.05\ N$ Configuration-1 shows approximately 75% improvement from the NTMD, whereas Configuration-2 shows a 73% improvement from the NTMD. This further implies that Configuration-1 also shows a 0.8% improvement from Configuration-2. These results indicate that Configuration-1 of the proposed NERS-TMDI is more effective for vibration reduction. Similar findings are observed for $F = 0.062\ N$ in Fig. 3(b). From Fig. 3(b), we observe that Configuration-1 shows a 75% improvement, whereas Configuration-2 shows a 52% improvement over NTMD. Additionally, Configuration-1 shows 15% improvement from Configuration-2. The performance improvement of Configuration-1 relative to Configuration-2 will be discussed in the later part of the analysis.

In the next step, we compare the performance of NERS-TMDI configurations to the linear optimal ERS-TMDI [42], and the results are shown in Fig. 4. Fig. 4(a) and (b) show the response of the primary system for each configuration and the ERS-TMDI with forcing amplitude of $F = 0.05\ N$ and $F = 0.062\ N$, respectively. From these figures, we can observe that Configuration-1 performs better than Configuration-2, and the ERS-TMDI. From Fig. 4(a), it can be easily observed that there is no significant difference in the performance of Configuration-1, Configuration-2, and the ERS-TMDI for $F = 0.05\ N$. More specifically, Configuration-1 provides a 0.3% improvement over ERS-TMDI and a 0.8% over Configuration-2. However, as the forcing amplitude increases from $F = 0.05\ N$ to $F = 0.062\ N$, the third resonant peak of the frequency response grows nota-

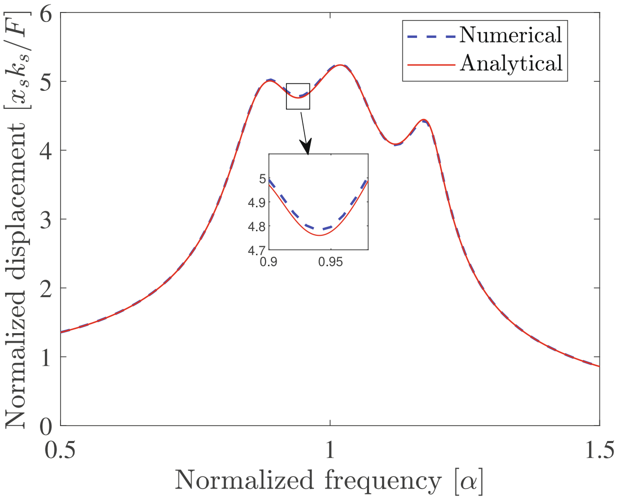

Fig. 2. A comparison between analytical and numerical simulation for Configuration-1 of NERS- TMDI to establish the accuracy of analytical approach for the grounded NERS-TMDI with $F = 0.05\ N$. The parameters for the primary system are $m_s = 1\ kg$, $k_s = 1\ N/m$, $k_{sn} = 1\ N/m^3$ and $c_s = 0.01\ Ns/m$.

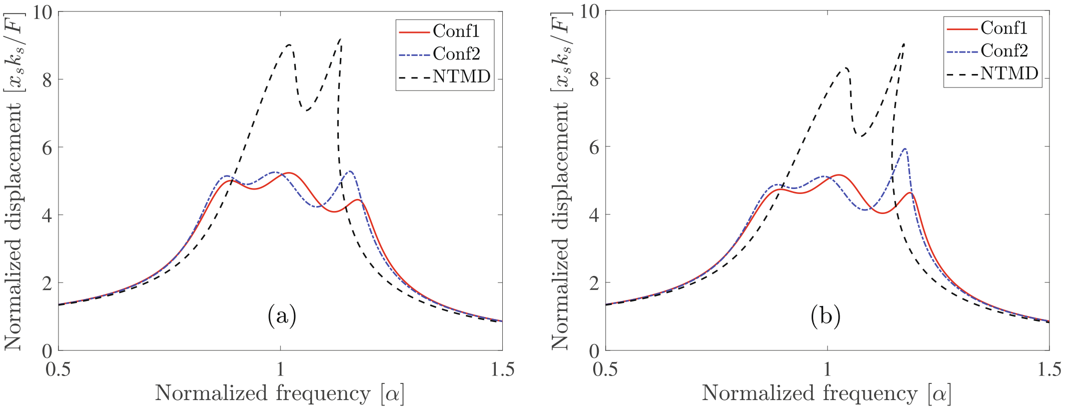

Fig. 3. Comparing the optimal frequency response of the classical NTMD to the NERS-TMDI configurations where the mass ratio μ = 0.02 for (a) *F* = 0.05 *N* and (b) *F* = 0.062 *N* . The other parameters for the primary system are m_s = 1 *kg*, k_s = 1 *N/m*, k_{sn} = 1 *N/m*^{3} and c_s = 0.01 *Ns/m*.

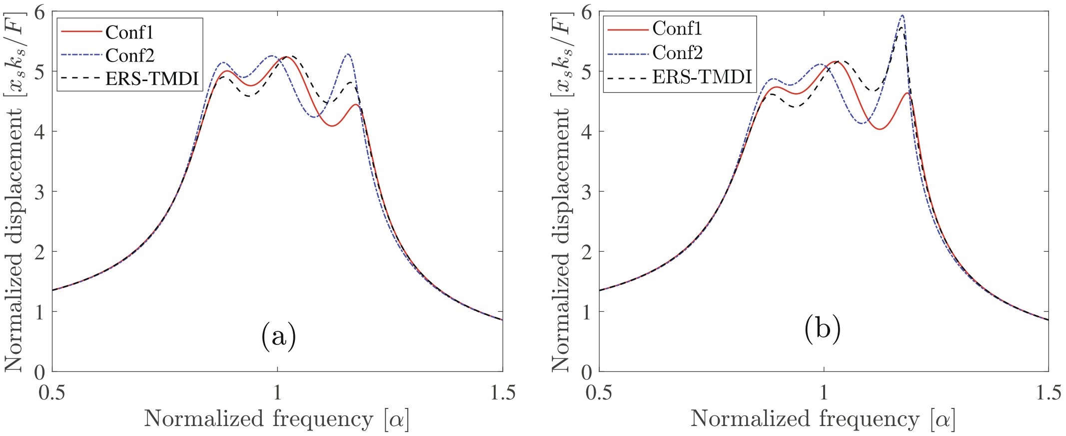

Fig. 4. Comparison of the optimal frequency response between the linear ERS-TMDI [42] and the NERS-TMDI configurations for (a) *F* = 0.05 *N* and (b) *F* = 0.062 *N*. The other parameters for the primary system are m_s = 1 *kg*, k_s = 1 *N/m*, k_{sn} = 1 *N/m*^{3} and c_s = 0.01 *Ns/m*.

Table 2
Parameters for Configuration-2 of the NERS-TMDI.

$m_t[kg]$	$b[kg]$	$k_t[N/m]$	$k_{tn}[N/m^3]$	k_f	$R(\Omega)$	$L(H)$	$C[F]$
0.02	0.02	0.0381	0.00074	0.055	0.3426	0.99	1.02

Table 3
Parameters of the NTMD.

$m_t[kg]$	$k_t[N/m]$	$k_{tn}[N/m^3]$	$c_t[N\ s/m]$
0.02	0.0192	0.00074	0.0034

bly larger than the other peaks, as can be seen in Fig. 4(b). In this case, Configuration-1 shows a 10% improvement over the ERS-TMDI, and a 15% over Configuration-2, implying an improved performance of Configuration-1 of the NERS-TMDI over the ERS-TMDI.

Having established the efficacy of the NERS-TMDI over the classical NTMD and the traditional ERS-TMDI for a nonlinear oscillator, next we compare the performance of Configuration-1 and Configuration-2 of NERS-TMDI. The main objective of this task is to ascertain the best configuration that can achieve efficient vibration mitigation and energy harvesting simultaneously. For this, we compare the frequency response curves corresponding to the normalized displacement of the primary structure (Fig. 5) and the normalized harvested power (Fig. 6). Since nonlinear oscillators are sensitive to the amplitude of external excitation, we analyze the performance of both configurations at different (increasing) values of excitation ampli-

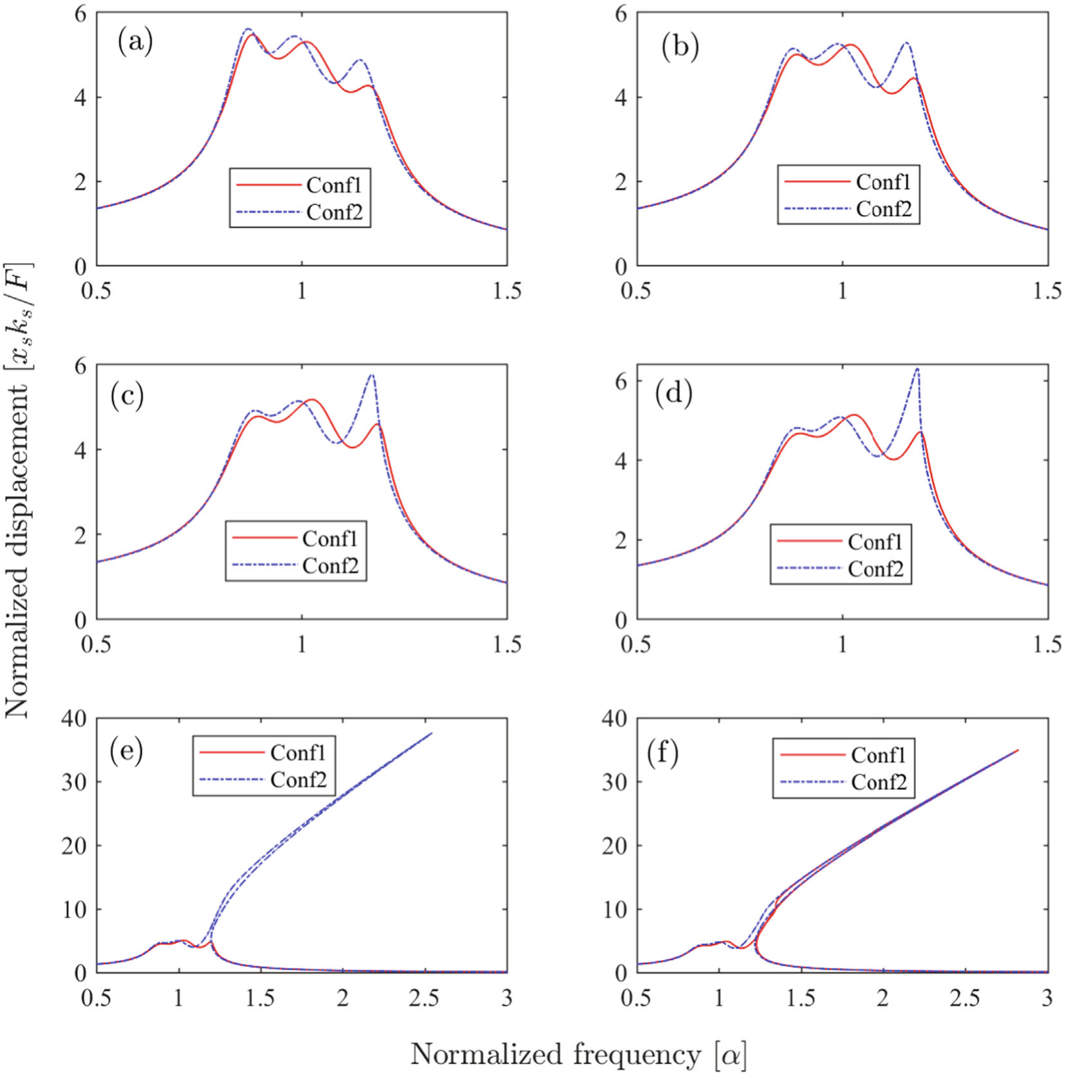

Fig. 5. Comparing the optimal frequency response of the NERS-TMDI configurations for (a) $F = 0.03\ N$, (b) $F = 0.05\ N$, (c)$F = 0.06\ N$, (d) $F = 0.065\ N$, (e) $F = 0.07\ N$, and (f)$F = 0.085\ N$. The other parameters for the primary system are $m_s = 1\ kg$, $k_s = 1\ N/m$, $k_{sn} = 1\ N/m^3$ and $c_s = 0.01\ Ns/m$.

tude. Fig. 5 shows the comparison between the frequency spectrums of the normalized displacement of the primary structure for Configuration-1 and Configuration-2 as a function of increasing forcing amplitude. We observe that irrespective of the excitation amplitude, the normalized displacement of the primary structure for Configuration-1 is smaller than that of Configuration-2. For example, Configuration-1 shows a 0.8% and a 15% improvement from Configuration-2 for $F = 0.05\ N$ and $F = 0.06\ N$, respectively. This increase in improvement can be further explained by the growth of the third resonant peak of the frequency response curve. From Fig. 5, we can easily observe that as the forcing amplitude increases, the third resonant peak of the response grows significantly for both configurations as compared to the other peaks. This notable growth in the third resonant peak of the response curve can be attributed to the inherent nonlinearity of the primary system, which becomes more visible as the forcing amplitude increases. Note that for Configuration-2, forcing amplitudes $F \geq 0.065\ N$ cause a tenfold increase in the third resonant peak compared to other peaks in the response. However, for Configuration-1, this sudden increase in the third resonant peak can be observed at higher forcing amplitudes, i.e., $F = 0.085\ N$. These excitation amplitude values, i.e., $F = 0.085\ N$ and $F = 0.065\ N$, represent threshold values for Configuration-1 and Configuration-2, respectively, beyond which the normalized displacement of the primary structure increases significantly. We emphasize that this significant increase in displacement presents an unacceptable solution for the NERS-TMDI configurations in both cases. In these instances, both configurations become ineffective for vibration control. However, as Configuration-1 can maintain acceptable vibration amplitudes for a relatively larger range of forcing amplitudes, it exhibits more applicability than Configuration-2. Hence, Configuration-1 of the NERS-TMDI would be the configuration of choice for better vibration reduction of the nonlinear oscillator as it is the most effective over a wider range of forcing amplitudes.

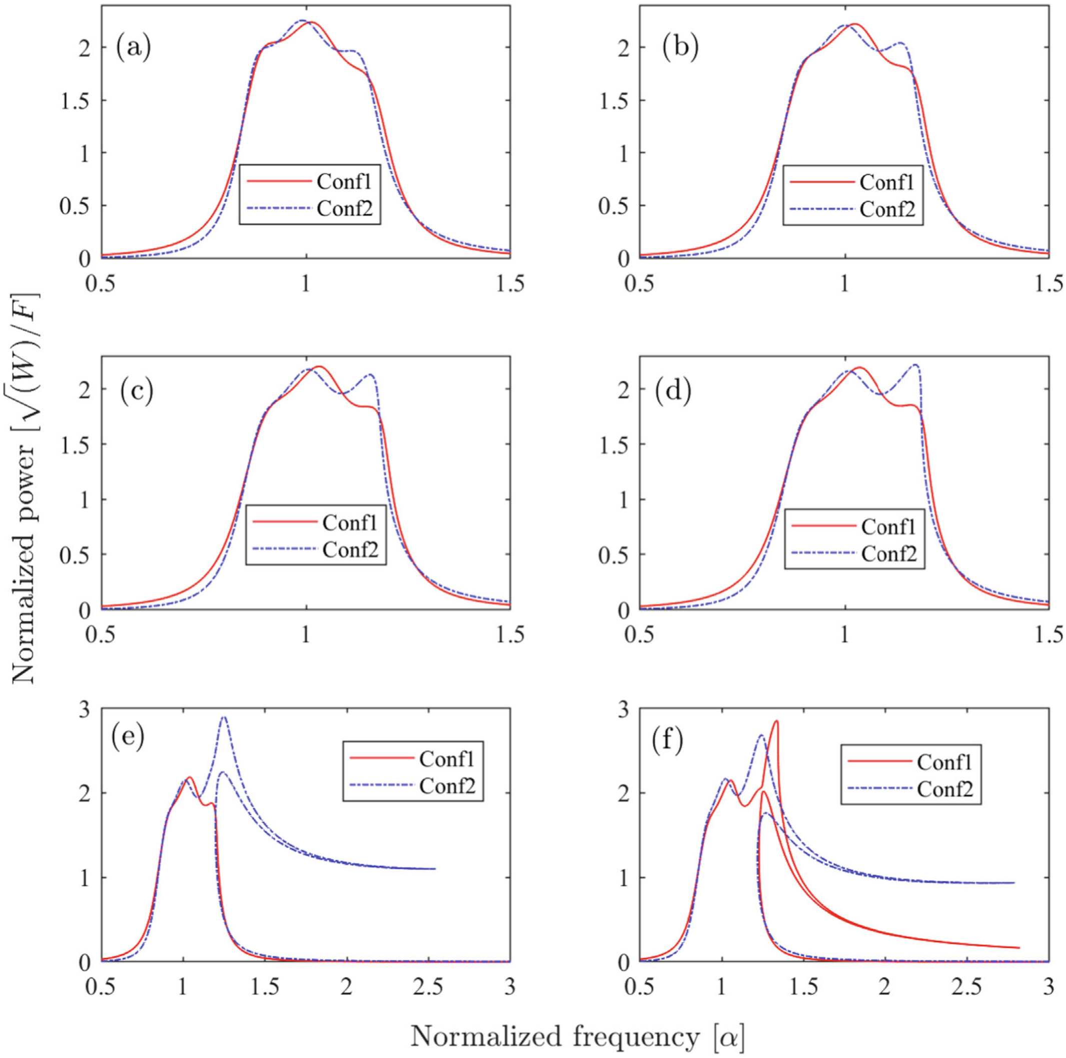

Fig. 6. Comparing the normalized power as a function of the normalized frequency of the NERS-TMDI configurations for (a) $F = 0.03$ N , (b) $F = 0.05$ N , (c) $F = 0.06$ N , (d) $F = 0.065$ N ,(e) $F = 0.07$ N , and (f)$F = 0.085$ N . The other parameters for the primary system are $m_s = 1$ kg, $k_s = 1$ N/m, $k_{sn} = 1$ N/m^3 and $c_s = 0.01$ Ns/m.

In the next step towards selecting an optimal configuration, we compare the performance of both configurations of the NERS-TMDI in terms of energy harvesting. For this, we evaluate the frequency spectrum of the normalized power generated by both configurations of the NERS-TMDI at different excitation amplitudes, and the results are shown in Fig. 6. We emphasize that the energy is being harvested simultaneously with the vibration mitigation of the primary structure for each configuration. Therefore, selecting an optimal configuration that can efficiently perform both tasks is critical and must be performed carefully. For example, for $F = 0.03$ N, Fig. 5(a) shows vibration mitigation for the normalized frequency interval $\alpha = 0.5$–1.5. For the same frequency interval, Fig. 6(a) shows the normalized power generated by the electromagnetic device. Although for $F = 0.03$ N, Configuration-1 performs significantly better for vibration mitigation as compared to Configuration-2, it performs slightly better (less than 1%) than Configuration-2 in terms of energy harvesting. Note that this observation is valid for low forcing amplitude, as can be seen from Fig. 6(a)-(b). However, as the excitation amplitude reaches towards $F = 0.065$ N, the third resonant peak in the response curve for Configuration-2 starts increasing and becomes dominant with values $F \geq 0.065$ N (Fig. 6(e)-(f)). A similar observation can be drawn for Configuration-1 with an excitation amplitude of $F = 0.085$ N. This notable increase in the third resonant peak leads to an increase in harvested power. However, these values of excitation amplitudes, i.e., $F = 0.085$ N and $F = 0.065$ N also represent the threshold values for Configuration-1 and Configuration-2, respectively, beyond which these absorbers will be ineffective for vibration mitigation. Therefore, we can only consider normalized power in the forcing amplitude region where the normalized displacement is acceptable, i.e., $F \leq 0.085$ N and $F \leq 0.065$ N for Configuration-1 and Configuration-2, respectively. Using these observations, we can conclude that although Configuration-1 is less efficient for energy harvesting than Configuration-2 around $F = 0.065$ N , it can sustain efficient simultaneous vibration control and energy harvesting for a relatively larger range of forcing amplitude, i.e., up to $F = 0.085\ N$.

3.3. Sensitivity analysis

In the next step towards the optimal designing of NERS-TMDI, we focus on identifying the effects of variation in the design parameters of NERS-TMDI. Since we have already established that Configuration-1 of NERS-TMDI performs better than Configuration-2, we present this analysis for Configuration-1 only.

In real-life applications, the tuned/optimum parameters of the proposed NERS-TMDI may vary over time and affect the performance of NERS-TMDI. To assess the effect of variation in the tuned/optimum parameters on the performance of the NERS-TMDI, we perform a sensitivity analysis for the design parameters of Configuration-1 of the NERS-TMDI. Fig. 7 shows the effects of ±15% variations from the tuned/optimum value of the nonlinear stiffness, k_{tn}, of NERS-TMDI on (a) the normalized displacement of the primary structure (Fig. 7(a)), and (b) the normalized harvested power of the electromagnetic device (Fig. 7(b)). We observe that increasing the nonlinear stiffness from its tuned/optimum value reduces the third resonant peak for both normalized displacement and normalized harvested power. Meanwhile decreasing it from its tuned/optimum value has an opposite effect on the performance of the NERS-TMDI as can be seen from Fig. 7(a)) and (b). However, it can be noted that these variations in k_{tn} do not significantly degrade the performance of the NERS-TMDI in terms of vibration mitigation and energy harvesting as can be seen from Fig. 7(a)) and (b).

Fig. 8 shows the effect of ±15% variations in the tuned/optimum inerter value b on the performance of Configuration-1 of NERS-TMDI. From Fig. 8, we can observe that an increase in the inertance from its tuned/optimum value degrades the performance of the NERS-TMDI as the third resonant peak in the frequency spectrum of normalized displacement grows significantly for the given value of excitation amplitude. Although the normalized harvested power increases with the increase in inertance, it cannot be selected as a feasible solution as it is a detriment to the vibration mitigation. On the other end, decreasing the inertance reduces the third resonant peak in the normalized displacement's frequency spectrum. However, the maximum normalized displacement of the primary system for this value of inerter remains higher than the case for the tuned/optimum value of inerter. Furthermore, the effective frequency range for normalized harvested power also decreases with any variation in the tuned/optimum inerter value. Therefore, it can be concluded that any variation in the tuned/optimum inerter value will degrade the performance of the NERS-TMDI significantly.

On a similar line, Fig. 9 shows the effect of ±15% variations in the tuned/optimum resistance value R on the performance of NERS-TMDI's Configuration-1. We can observe that an increase in the resistance causes an increase in the third resonant peak of the normalized displacement of the primary structure, which further increases the rate at which the system becomes unstable as the forcing amplitude increases. Also, the increase in resistance from its tuned/optimum value reduces the maximum normalized harvested power. Meanwhile, decreasing the resistance from its optimal value increases the normalized displacement of the primary structure as well as the normalized harvested power. However, we cannot use this as a feasible solution because of its cost to the vibration mitigation. Therefore, any variation in tuned value of resistance will also degrade the performance of the tuned NERS-TMDI as observed in the case of inerter.

Proceeding further, Fig. 10 shows the effect of ±15% variations in the tuned/optimum inductance value L on the performance of proposed NERS-TMDI. From Fig. 10(a) and (b), we can observe that an increase in the tuned/optimum value of inductance causes the merge of the second resonant peak with the first or third resonant peak, thus generating only two peaks in the frequency spectrum. Additionally, it causes a notable growth in the resonance peak. Decreasing the inductance from its tuned/optimum value also causes merging of the resonant peaks, thus producing only two peaks in the frequency spectrum. Note that in both variations, we observe an increase in the maximum normalized displacement as well as in the

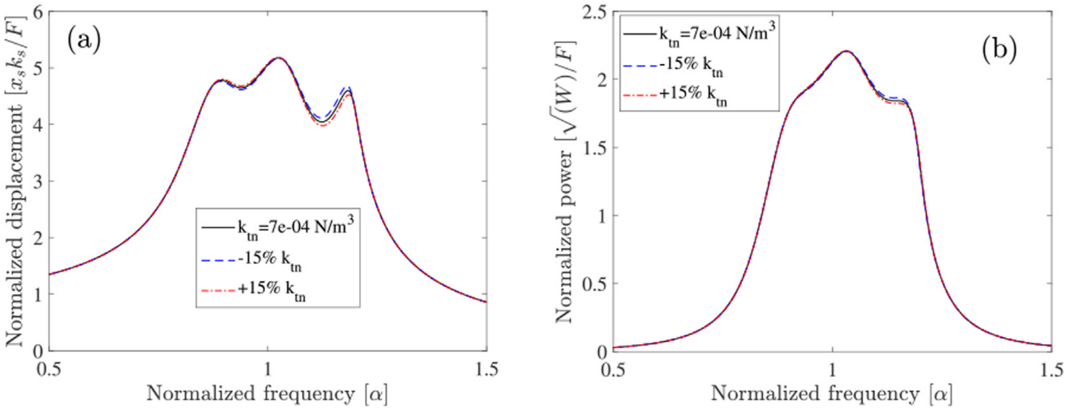

Fig. 7. Evaluating the sensitivity of the system relative to the nonlinear stiffness of the NERS-TMDI for: (a) the normalized displacement and (b) the normalized power at $F = 0.06\ N$. The parameters for the primary system are $m_s = 1\ kg$, $k_s = 1\ N/m$, $k_{sn} = 1\ N/m^3$ and $c_s = 0.01\ Ns/m$.

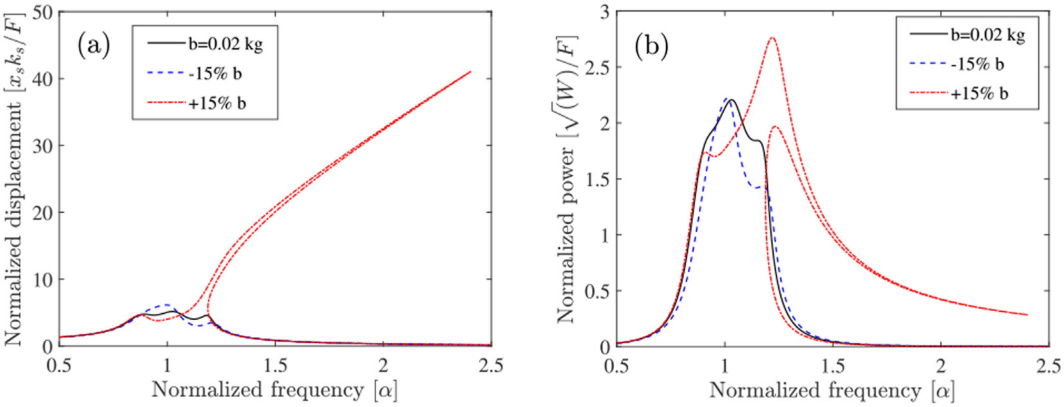

Fig. 8. Evaluating the sensitivity of the system relative to the inerter magnitude of the NERS-TMDI for: (a) the normalized displacement and (b) the normalized power at $F = 0.06$ *N*. The parameters for the primary system are $m_s = 1$ *kg*, $k_s = 1$ *N/m*, $k_{sn} = 1$ *N/m*^{3} and $c_s = 0.01$ *Ns/m*.

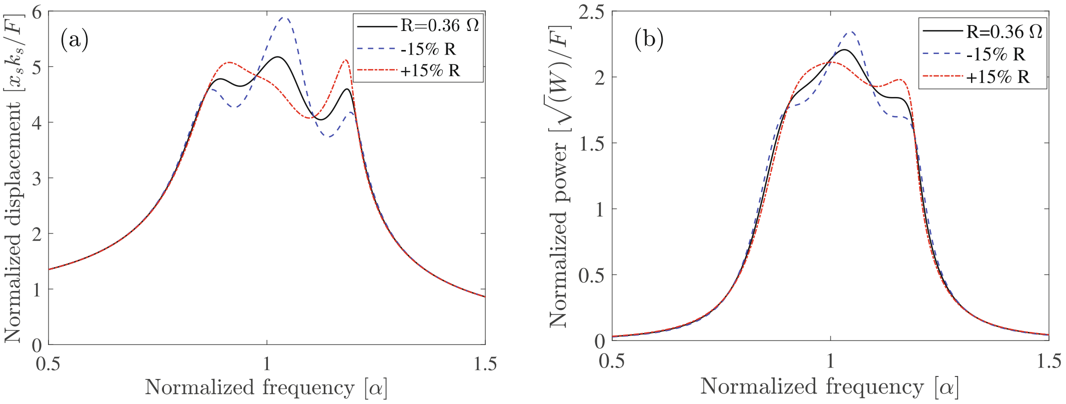

Fig. 9. Evaluating the sensitivity of the system relative to the resistance of the NERS-TMDI for: (a) the normalized displacement and (b) the normalized power at $F = 0.06$ *N* . The parameters for the primary system are $m_s = 1$ *kg*, $k_s = 1$ *N/m*, $k_{sn} = 1$ *N/m*^{3} and $c_t = 0.01$ *Ns/m*.

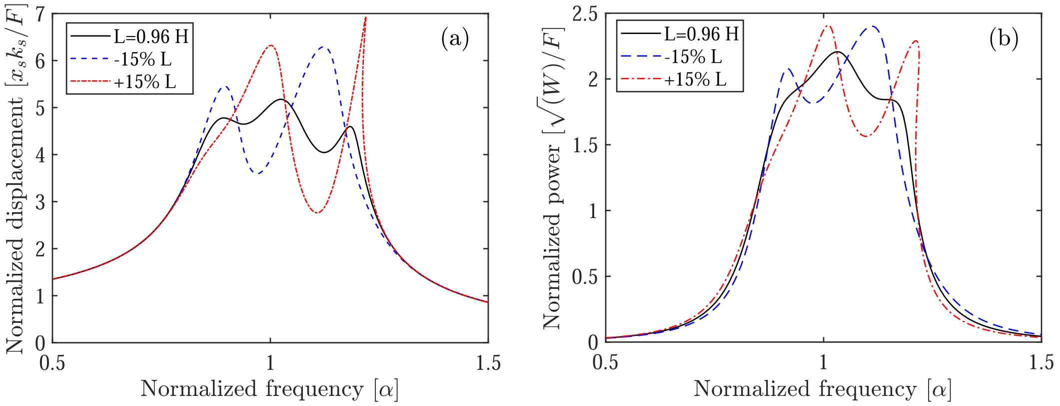

Fig. 10. Evaluating the sensitivity of the system relative to the inductance of the NERS-TMDI for:(a) the normalized displacement and (b) the normalized power at $F = 0.06$ *N*. The parameters for the primary system are $m_s = 1$ *kg*, $k_s = 1$ *N/m*, $k_{sn} = 1$ *N/m*^{3} and $c_s = 0.01$ *Ns/m*.

maximum normalized harvested power. However, the increase in normalized power coincides with an increase in normalized displacement, and hence, cannot be selected as a feasible solution. Finally, we present the effect of variation in the optimal value of capacitance value, *C*, on the performance of Configuration-1 of NERS-TMDI, and the results are shown in Fig. 11. From Fig. 11, we can obverse that the effects of ±15% variations in the tuned/optimum capacitance value on the performance

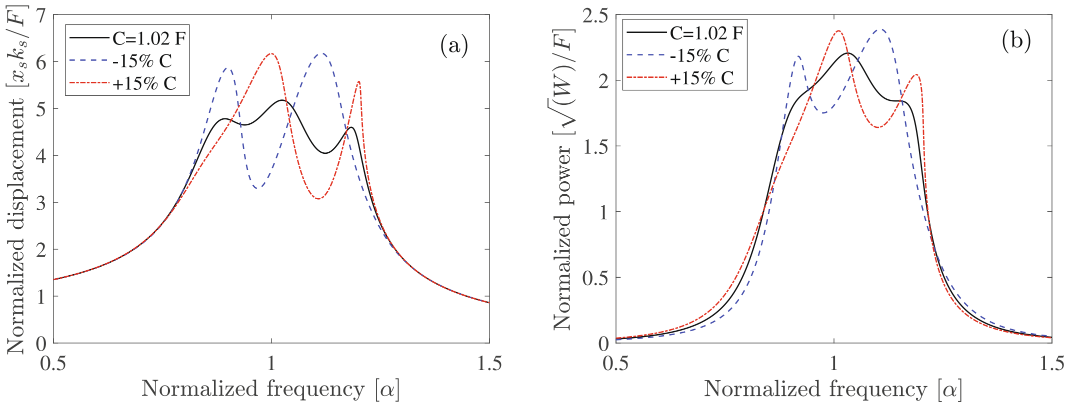

Fig. 11. Evaluating the sensitivity of the system relative to the capacitance of the NERS-TMDI for: (a) the normalized displacement and (b) the normalized power at $F = 0.06$ N . The parameters for the primary system are $m_s = 1$ kg, $k_s = 1$ N/m, $k_{sn} = 1$ N/m^3 and $c_s = 0.01$ Ns/m.

of NERS-TMDI are very similar to that of the inductance variations. Therefore, we can conclude that any variation in inductance and capacitance degrades the performance of the NERS-TMDI in a similar fashion.

In brief, the nonlinear stiffness of the proposed NERS-TMDI is very robust to perturbations around its optimal value. However, variations in the inertance, the resistance, the inductance, and the capacitance degrade the performance of the NERS-TMDI by significantly changing its dynamics in terms of vibration control and energy harvesting.

3.4. Parametric study for optimal energy harvesting

The sensitivity analysis reveals the effect of variation in the design parameters around their tuned/optimal values on the performance of NERS-TMDI in terms of vibration control and energy harvesting. However, another approach to determine the critical design parameter of the NERS-TMDI for optimal energy harvesting is to excite the primary structure by an impulse input, i.e., $\dot{x}_s(0) = 0$, which further implies $F_w = 0$. The motivation of this approach is to excite all the modes of the coupled system simultaneously and observe the behavior of the NERS-TMDI. In doing so, it is possible to determine the energy harvested in terms of the kinetic energy of the primary structure using the following equation

$$E_{har,\%} = 100\frac{\int_0^t (RI^2(\tau))d\tau}{\int_0^t \frac{1}{2}m_s\dot{x}_s(0)d\tau} \tag{5}$$

Using Eq. (5), it is possible to evaluate the energy harvested by the system as a function of the NERS-TMDI parameters and the impulse amplitude. This methodology is similar to the one developed by Viguie *et al.* [48], where the dissipated energy in the optimal NTVA is evaluated as a function of the nonlinear stiffness of the primary structure. We use this methodology to determine the effects of the parameters on the amount of energy harvested as the impulse increases. For the following energy simulations, we consider a weakly damped primary structure (i,e $c_s = 0.002$ Ns/m) to induce energy harvesting.

We start our parametric analysis with the nonlinear stiffness of the NERS-TMDI, and its effect on the harvested energy has been shown in Fig. 12. In Fig. 12, the effect of k_{tn} along with impulse magnitude on the harvested energy has been shown using three-dimensional energy graph and corresponding contour. The results show that for lower values of nonlinear stiffness, as the impulse amplitude increases, the energy harvested drops to near zero, and the NERS-TMDI loses its effectiveness. However, with an increase in the nonlinear stiffness, the major portion (i,e 90%) of the initial energy is harvested with increasing impulse amplitude.

We now focus on the impact of the inerter on the performance of the NERS-TMDI. Fig. 13 shows the three-dimensional energy graph of the energy harvested by the NERS-TMDI as a function of the impulse amplitude and the inerter magnitude. From Fig. 13, we can observe that as the impulse amplitude increases from $\dot{x}_s(0) = 0$ m/s to $\dot{x}_s(0) = 3$ m/s, a major portion of the initial energy will get harvested irrespective of the value of inerter. However, with a further increase in impulse from $\dot{x}_s(0) = 3$-m/s, the efficiency of the NERS-TMDI for energy harvesting gradually drops to 70% for smaller values of inerter (less than *0*.005). Note that this drop in efficiency is observed for all values of inerter; however, the transition impulse point, corresponding to the decrease in efficiency, increases with an increase in inerter magnitude. Therefore, the drop in the efficiency is observed for higher impulse amplitude at high values of inerter. This observation further implies that a NERS-TMDI configuration with a higher inerter value will be able to maintain high energy harvesting levels for a wider range of impulse amplitude.

Proceeding further, Fig. 14 shows the three-dimensional energy graph of the energy harvested by the NERS-TMDI as a function of the impulse amplitude and the resistance. From Fig. 14, we can observe that in a range of $R = 0.2$–1 Ω, up to 90% of the energy is harvested for impulse amplitude $\dot{x}_s$ 3. However, with a further increase in $\dot{x}_s(0)$ from 3 m/s, the harvested

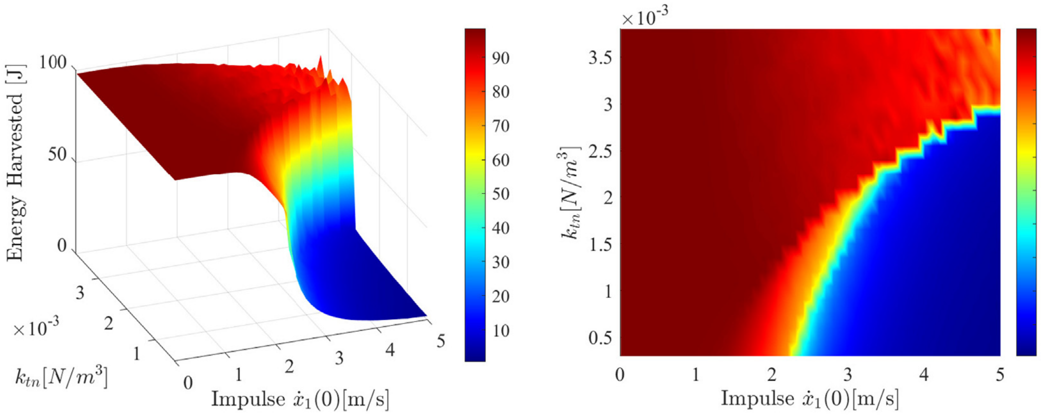

(a) (b)

Fig. 12. Energy harvested in Configuration-1 of the NERS-TMDI against the nonlinear stiffness and the impulse magnitude: (a) three-dimensional graph and (b) contour plot. The parameters for the primary system are m_s = 1 *kg*, k_s = 1 *N/m*, k_{sn} = 1 *N/m*^{3} and c_s = 0.002 *Ns/m*.

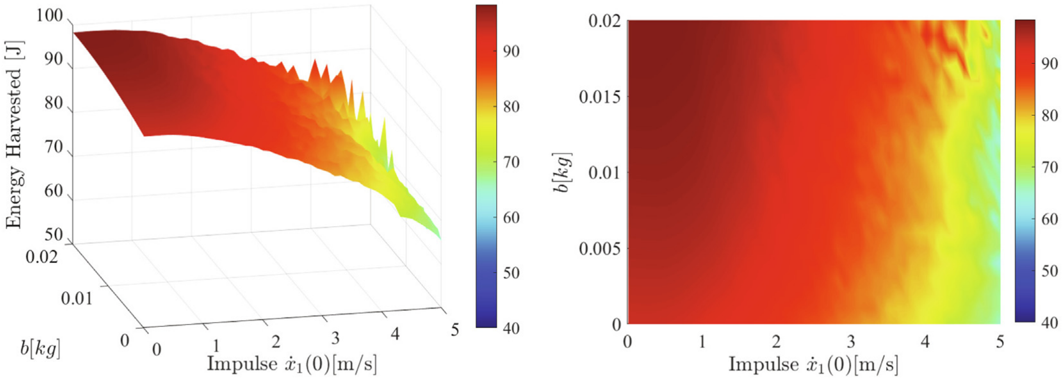

(a) (b)

Fig. 13. Energy harvested in Configuration-1 of the NERS-TMDI against the inerter magnitude and the impulse magnitude: (a) three-dimensional graph and (b) contour plot. The parameters for the primary system are m_s = 1 *kg*, k_s = 1 *N/m*, k_{sn} = 1 *N/m*^{3} and c_s = 0.002 *Ns/m*.

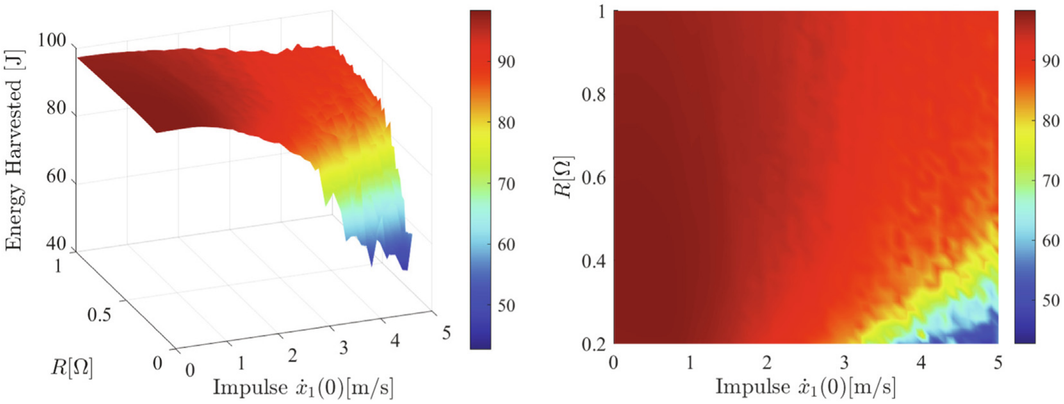

(a) (b)

Fig. 14. Energy harvested in Configuration-1 of the NERS-TMDI against the resistance and the impulse magnitude: (a) three-dimensional graph and (b) contour plot. The parameters for the primary system are m_s = 1 *kg*, k_s = 1 *N/m*, k_{sn} = 1 *N/m*^{3} and c_s = 0.002 *Ns/m*.

energy drops to 50% for $R = 0.2\ \Omega$. Similar to the case of inerter, the transition impulse point, corresponding to the decrease in efficiency, increases with an increase in the magnitude of resistance. However, unlike in the case of the inerter, the transition point increases gradually. Therefore, in a range of $\dot{x}_s(0) = 0–5\ m/s$, $R \geq 0.4\ \Omega$ will be sufficient to harvest 90% of the initial energy.

Fig. 15 shows the three-dimensional energy graph of the energy harvested by the NERS-TMDI as a function of the impulse amplitude and the inductance. The figure shows that for amplitude $\dot{x}_s(0)$ smaller than 2 m/s, a major portion of the energy is harvested regardless of the inductance value. However, this transition impulse point increase with a decrease in the value of the inductance. This observation is contrary to earlier cases of parameters, where the transition impulse point increases with an increase in parameter value. This further implies that the inductance should be maintained at lower values to ensure significant energy harvesting for a wider range of impulse amplitudes. Finally, Fig. 16 shows the three-dimensional energy graph of the energy harvested by the NERS-TMDI as a function of the impulse amplitude and the capacitance. The plot has a similar trend than the inductance energy plot. We observe that lower values of capacitance can maintain a considerable value of energy harvesting as the impulse amplitude increases.

4. Discussion

The analytical and numerical simulations along with the sensitivity analysis provide good insights into the performance of the proposed NERS-TMDI configurations. We observed that, if applied to the nonlinear systems, the NERS-TMDI configurations are superior to the existing alternatives, i.e., the conventional NTMD and the ERS-TMDI in terms of vibration control.

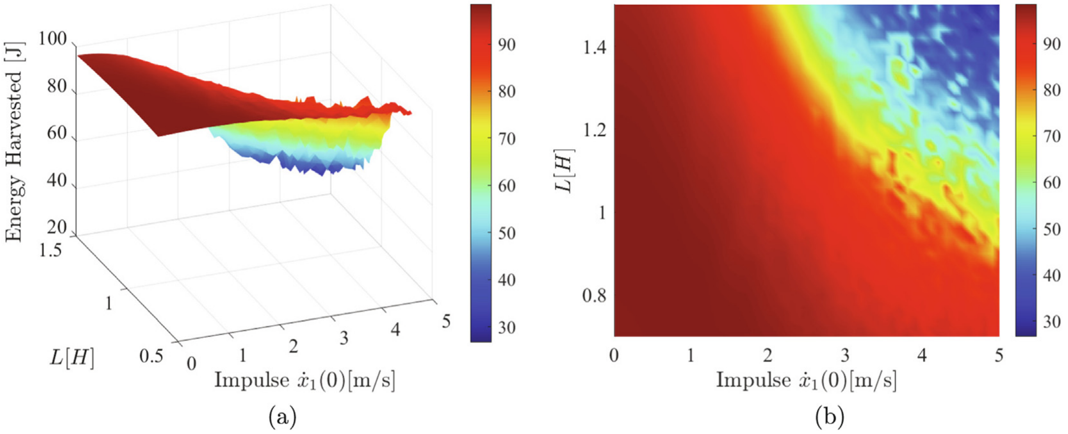

Fig. 15. Energy harvested in Configuration-1 of the NERS-TMDI against the inductance and the impulse magnitude: (a) three-dimensional graph and (b) contour plot. The other parameters for the primary system are $m_s = 1\ kg$, $k_s = 1\ N/m$, $k_{sn} = 1\ N/m^3$ and $c_s = 0.002\ Ns/m$.

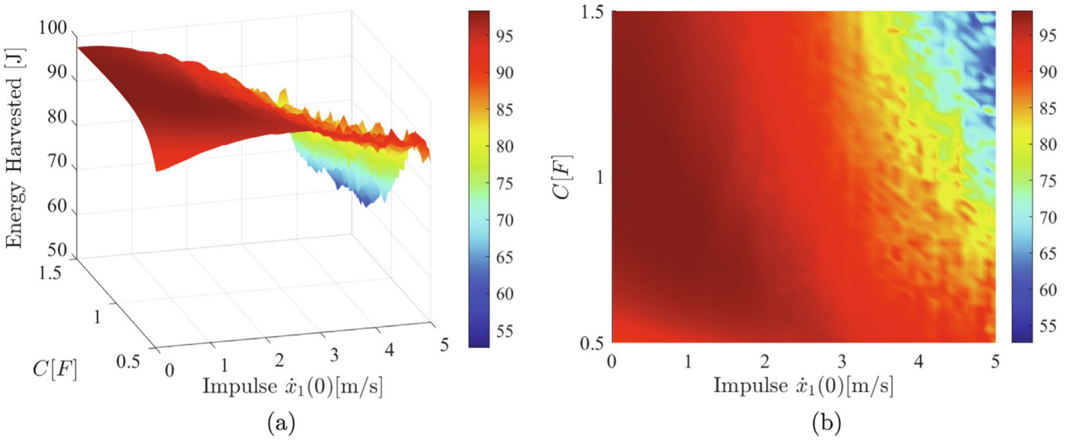

Fig. 16. Energy harvested in Configuration-1 of the NERS-TMDI against the capacitance and the impulse magnitude: (a) three-dimensional graph and (b) contour plot. The parameters for the primary system are $m_s = 1\ kg$, $k_s = 1\ N/m$, $k_{sn} = 1\ N/m^3$ and $c_s = 0.002\ Ns/m$.

We also observed that Configuration-1 is superior to Configuration-2 as it can maintain sustainable energy harvesting while mitigating the mechanical vibrations for a relatively wider range of forcing amplitude. For a given system and tuned NERS-TMDI parameters, Configuration-1 can achieve both vibration control and energy harvesting from $F = 0\ N$ to $F = 0.085\ N$, whereas for Configuration-2 it extends to $F = 0.065\ N$. We were also able to establish that higher nonlinear stiffness, inerter magnitude and resistance along with lower capacitance and inductance can significantly improve the performance of the NERS-TMDI for energy harvesting in the case of initial impulse excitation. In addition, the sensitivity analysis showed that increasing the nonlinear stiffness improves vibration control while maintaining the maximum energy harvested for a selected force. These results also indicate that varying other parameters from its tuned/optimal value will degrade the performance of the NERS-TMDI.

5. Conclusion and remarks

In this work, for the first time, we propose two nonlinear electromagnetic resonant shunt tuned mass damper-inerter (NERS-TMDI) configurations for simultaneous vibration reduction and energy harvesting for a nonlinear oscillator, under external excitation. The considered nonlinear oscillator is modeled as a Duffing oscillator. Two optimal linear ERS-TMDI are extended to NERS-TMDI following the nonlinear vibration absorber tuning methodology. In Configuration-1 the electromagnetic device is grounded while in Configuration-2 the electromagnetic device is sandwiched between the primary mass and the tuned absorber's mass. The analytical solutions are obtained using the harmonic balance method, and are further validated against numerical simulations. The numerical examples help establish the following findings:

a) If applied to a Duffing oscillator, the proposed NERS-TMDI configurations are better than the optimal nonlinear tuned mass damper (NTMD) as well as the optimal ERS-RMDI for increasing amplitudes.
b) There exists a forcing amplitude threshold beyond which the nonlinear dynamics of the primary structure cause a significant growth in displacement and degrades the performance of NERS-TMDI.
c) Comparison between two configurations of NERS-TMDI shows the superiority of Configuration-1 over Configuration-2 as Configuration-1 exhibits higher range of feasible forcing without degrading the performance.
d) A detailed analysis of the optimal Configuration-1 demonstrates that the performance of the NERS-TMDI for energy harvesting is improved for higher nonlinear stiffness, inerter magnitude and resistance, and for lower capacitance and inductance.
e) A sensitivity analysis near the tuned/optimum parameter values of Configuration-1 showes that the device is robust to variations in nonlinear stiffness. However, variations in inertance, resistance, inductance, and capacitance significantly degrade the performance of the NERS-TMDI.

Stability and bifurcation analysis of the proposed NERS-TMDI is left for future work. Future work will also involve developing a rigorous optimization scheme to improve the current solution for the NERS-TMDI. Finally, the results will be experimentally validated.

CRediT authorship contribution statement

Paul Kakou: Conceptualization, Methodology, Software, Validation, Formal analysis, Investigation, Writing - original draft, Visualization. **Oumar Barry:** Conceptualization, Methodology, Investigation, Resources, Writing - review & editing, Visualization, Supervision, Project administration, Funding acquisition.

Declaration of Competing Interest

The authors declare that they have no known competing financial interests or personal relationships that could have appeared to influence the work reported in this paper.

Acknowledgment

This work is supported in part by by the National Science Foundation (NSF) Grant ECCS-1944032: CAREER: Towards a Self-Powered Autonomous Robot for Intelligent Power Lines Vibration Control and Monitoring.

References

[1] Ki-Jun Seong, Ho-Gyun Kang, Bo-Yeon Yeo, Ho-Pyeong Lee, The stabilization loop design for a two-axis gimbal system using lqg/ltr controller, in: 2006 SICE-ICASE International Joint Conference, IEEE, 2006, pp. 755–759.
[2] Hamed Khodadadi, Mohammad Reza Jahed Motlagh, Mohammad Gorji, Robust control and modeling a 2-dof inertial stabilized platform, in: International Conference on Electrical, Control and Computer Engineering 2011 (InECCE), IEEE, 2011, pp. 223–228.
[3] Aytac Altan, Rifat Hacioglu, Hammerstein model performance of three axes gimbal system on unmanned aerial vehicle (uav) for route tracking, in: 2018 26th Signal Processing and Communications Applications Conference (SIU), IEEE, 2018, pp. 1–4.

[4] Aytac Altan, Rıfat Hacıoğlu, Model predictive control of three-axis gimbal system mounted on uav for real-time target tracking under external disturbances, Mech. Syst. Sig. Process. 138 (2020) 106548.
[5] O. Barry, J.W. Zu, D.C.D. Oguamanam, Nonlinear dynamics of stockbridge dampers, J. Dyn. Syst., Measure., Control 137 (6) (2015) 061017.
[6] M.A. Bukhari, O. Barry, E. Tanbour, On the vibration analysis of power lines with moving dampers, J. Vib. Control 24 (18) (2018) 4096–4109.
[7] Krzysztof Kecik and Andrzej Mitura. Energy recovery from a pendulum tuned mass damper with two independent harvesting sources. International Journal of Mechanical Sciences, page 105568, 2020.
[8] Miao Yuan, Kefu Liu, Ayan Sadhu, Simultaneous vibration suppression and energy harvesting with a non-traditional vibration absorber, J. Intell. Mater. Syst. Struct. 29 (8) (2018) 1748–1763.
[9] Xiudong Tang, Lei Zuo, Simultaneous energy harvesting and vibration control of structures with tuned mass dampers, J. Intell. Mater. Syst. Struct. 23 (18) (2012) 2117–2127.
[10] Hermann Frahm. Device for damping vibrations of bodies., April 18 1911. US Patent 989,958.
[11] J.Q. Sun, M. Re Jolly, M.A. Norris, Passive, adaptive and active tuned vibration absorbers—a survey, J. Vib. Acoust. 117 (B) (1995) 234–242.
[12] M.H. Miguélez, L. Rubio, J.A. Loya, J. Fernández-Sáez, Improvement of chatter stability in boring operations with passive vibration absorbers, Int. J. Mech. Sci. 52 (10) (2010) 1376–1384.
[13] Matthew A. Lackner, Mario A. Rotea, Passive structural control of offshore wind turbines, Wind Energy 14 (3) (2011) 373–388.
[14] H. Moradi, F. Bakhtiari-Nejad, M.R. Movahhedy, Tuneable vibration absorber design to suppress vibrations: an application in boring manufacturing process, J. Sound Vib. 318 (1–2) (2008) 93–108.
[15] Jeong-Hoi Koo, Mehdi Ahmadian, Mehdi Setareh, Thomas Murray, In search of suitable control methods for semi-active tuned vibration absorbers, J. Vib. Control 10 (2) (2004) 163–174.
[16] N Jalili, A comparative study and analysis of semi-active vibration-control systems, J. Vib. Acoust. 124 (4) (2002) 593–605.
[17] Navid Asmari Saadabad, Hamed Moradi, Gholamreza Vossoughi, Semi-active control of forced oscillations in power transmission lines via optimum tuneable vibration absorbers, Int. J. Mech. Sci. 87 (2014) 163–178.
[18] Sanjiv G. Tewani, Keith E. Rouch, Bruce L. Walcott, A study of cutting process stability of a boring bar with active dynamic absorber, Int. J. Mach. Tools Manuf. 35 (1) (1995) 91–108.
[19] Malcolm John Hudson, Paul Reynolds, Implementation considerations for active vibration control in the design of floor structures, Eng. Struct. 44 (2012) 334–358.
[20] G.J. Liao, X.L. Gong, C.J. Kang, S.H. Xuan, The design of an active–adaptive tuned vibration absorber based on magnetorheological elastomer and its vibration attenuation performance, Smart Mater. Struct. 20 (7) (2011) 075015.
[21] J B Hunt, J -C Nissen, The broadband dynamic vibration absorber, JSV 83 (4) (1982) 573–578.
[22] P.L. Walsh, J.S. Lamancusa, A variable stiffness vibration absorber for minimization of transient vibrations, J. Sound Vib. 158 (2) (1992) 195–211.
[23] Malcolm C. Smith, Synthesis of mechanical networks: the inerter, IEEE Trans. Autom. Control 47 (10) (2002) 1648–1662.
[24] Michael Z.Q. Chen, Christos Papageorgiou, Frank Scheibe, Fu-Cheng Wang, Malcolm C. Smith, The missing mechanical circuit element, IEEE Circuits Syst. Mag. 9 (1) (2009) 10–26.
[25] Xu Kun, Kaiming Bi, Qiang Han, Xiaopeng Li, Du Xiuli, Using tuned mass damper inerter to mitigate vortex-induced vibration of long-span bridges: Analytical study, Eng. Struct. 182 (2019) 101–111.
[26] D. Pietrosanti, M. De Angelis, M. Basili, Optimal design and performance evaluation of systems with tuned mass damper inerter (tmdi), Earthquake Eng. Struct. Dyn. 46 (8) (2017) 1367–1388.
[27] Agathoklis Giaralis, Francesco Petrini, Wind-induced vibration mitigation in tall buildings using the tuned mass-damper-inerter, J. Struct. Eng. 143 (9) (2017) 04017127.
[28] Alexey Kuznetsov, Musa Mammadov, Ibrahim Sultan, Eldar Hajilarov, Optimization of improved suspension system with inerter device of the quarter-car model in vibration analysis, Arch. Appl. Mech. 81 (10) (2011) 1427–1437.
[29] Laurentiu Marian, Agathoklis Giaralis, Optimal design of a novel tuned mass-damper–inerter (tmdi) passive vibration control configuration for stochastically support-excited structural systems, Probab. Eng. Mech. 38 (2014) 156–164.
[30] Xin Dong, Yuance Liu, Michael Z.Q. Chen, Application of inerter to aircraft landing gear suspension, in: 2015 34th Chinese Control Conference (CCC), IEEE, 2015, pp. 2066–2071.
[31] Robert L. Forward, Electronic damping of vibrations in optical structures, Appl. Opt. 18 (5) (1979) 690–697.
[32] Nesbitt W. Hagood, Andreas von Flotow, Damping of structural vibrations with piezoelectric materials and passive electrical networks, J. Sound Vib. 146 (2) (1991) 243–268.
[33] S.O. Reza Moheimani, A survey of recent innovations in vibration damping and control using shunted piezoelectric transducers, IEEE Trans. Control Syst. Technol. 11 (4) (2003) 482–494.
[34] Ufuk Yigit, Ender Cigeroglu, Erhan Budak, Chatter reduction in boring process by using piezoelectric shunt damping with experimental verification, Mech. Syst. Sig. Process. 94 (2017) 312–321.
[35] A.J. Fleming, S. Behrens, S.O.R. Moheimani, Reducing the inductance requirements of piezoelectric shunt damping systems, Smart Mater. Struct. 12 (1) (2003) 57–64.
[36] Sam Behrens, Andrew J. Fleming, S.O. Reza Moheimani, Passive vibration control via electromagnetic shunt damping, IEEE/ASME Trans. Mechatron. 10 (1) (2005) 118–122.
[37] Tai-Hong Cheng, Oh Il-Kwon, A current-flowing electromagnetic shunt damper for multi-mode vibration control of cantilever beams, Smart Mater. Struct. 18 (9) (2009) 095036.
[38] Bo Yan, Hongye Ma, Yu Ning, Lu Zhang, Wu Chuanyu, Theoretical modeling and experimental analysis of nonlinear electromagnetic shunt damping, J. Sound Vib. 471 (2020) 115184.
[39] Lei Zuo, Wen Cui, Dual-functional energy-harvesting and vibration control: electromagnetic resonant shunt series tuned mass dampers, J. Vib. Acoust. 135 (5) (2013).
[40] Hongxin Sun, Yifan Luo, Xiuyong Wang, Lei Zuo, Seismic control of a sdof structure through electromagnetic resonant shunt tuned mass-damper-inerter and the exact h2 optimal solutions, J. Vibroengineering 19 (3) (2017) 2063–2079.
[41] Yifan Luo, Hongxin Sun, Xiuyong Wang, Lei Zuo, Ning Chen, Wind induced vibration control and energy harvesting of electromagnetic resonant shunt tuned mass-damper-inerter for building structures, Shock Vib. 2017 (2017) 1–13.
[42] Eshagh Farzaneh Joubaneh, Oumar Rafiou Barry, On the improvement of vibration mitigation and energy harvesting using electromagnetic vibration absorber-inerter: Exact h2 optimization, J. Vib. Acoust. 141 (6) (2019).
[43] David Wagg, S.A. Neild, Nonlinear vibration with control, Springer, 2016.
[44] Ali H. Nayfeh, Dean T. Mook, Nonlinear oscillations, John Wiley & Sons (2008).
[45] Xiuting Sun, Xu Jian, Feng Wang, Li Cheng, Design and experiment of nonlinear absorber for equal-peak and de-nonlinearity, J. Sound Vib. 449 (2019) 274–299.
[46] Giuseppe Habib, Thibaut Detroux, Régis Viguié, Gäetan Kerschen, Nonlinear generalization of den hartog's equal-peak method, Mech. Syst. Sig. Process. 52-53 (2015) 17–28.
[47] Pankaj Wahi, Anindya Chatterjee, Self-interrupted regenerative metal cutting in turning, Int. J. Non Linear Mech. 43 (2) (2008) 111–123.
[48] Régis Viguié, Maxime Peeters, Gäetan Kerschen, J.-C. Golinval, Energy transfer and dissipation in a duffing oscillator coupled to a nonlinear attachment, J. Comput. Nonlinear Dyn. 4 (4) (2009).